Enhanced magnetic halloysite nanotubes for dye removal at different pH conditions

Nguyen, Ngoc Quang; Jeong, Younhee; Abelmann, Leon; Ryu, Jungju; Sohn, Daewon

DOI
10.1016/j.colsurfa.2023.132631

Publication date
2024

Document Version
Final published version

Published in
Colloids and Surfaces A: Physicochemical and Engineering Aspects

Colloids and Surfaces A: Physicochemical and Engineering Aspects 680 (2024) 132631

Contents lists available at ScienceDirect

Colloids and Surfaces A: Physicochemical and Engineering Aspects

journal homepage: www.elsevier.com/locate/colsurfa

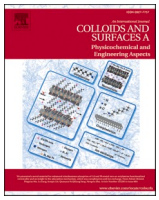

Enhanced magnetic halloysite nanotubes for dye removal at different pH conditions

Ngoc Quang Nguyen [a], Younhee Jeong [a], Leon Abelmann [b], Jungju Ryu [a], Daewon Sohn [a,*]

[a] Department of Chemistry and Research Institute for Convergence of Basic Science, Department of Chemistry, 222 Wangsimni-ro, Seoul 04763, South Korea
[b] KIST-Europe, Campus E7 1, 66123 Saarbrucken, Germany, and Department of Microelectronics, Technische Universiteit Delft, Mekelweg 5, Delft 2628 CD, Netherlands

HIGHLIGHTS

- The synthesis of magnetic halloysite nanotubes (HNTs) for eco-friendly clay.
- The dye removal model for bonding structures among magnetic HNTs and dyes.
- Different pH environments for the behavior of magnetic HNTs after dye absorption.
- Modified HNTs is promising for organic dye removal and wastewater treatment.

GRAPHICAL ABSTRACT

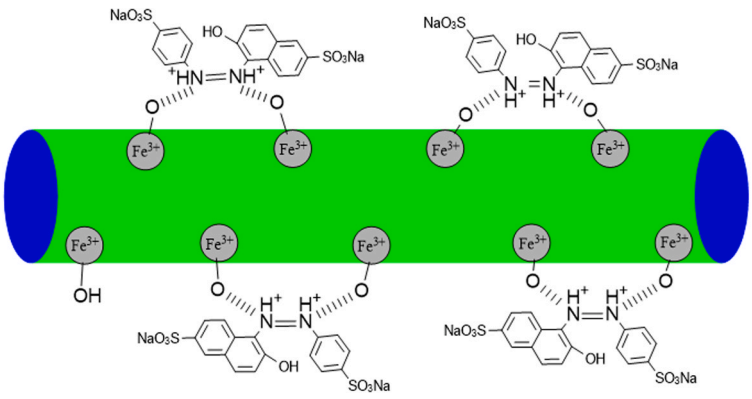

ARTICLE INFO

Keywords:
Halloysite
Nanotube
Magnetic particle
Dye adsorption
Dye removal

ABSTRACT

Halloysite nanotubes (HNTs) have been extensively investigated for potential utilization due to their unique structure and properties as a type of natural, eco-friendly clay. The synthesis and modification of magnetic halloysite nanotubes was studied using several experimental techniques including SEM, TEM, FT-IR, Raman spectroscopy, UV-Vis spectroscopy, and BET. Dye absorption experiments were conducted to understand bonding using EDS, XPS, XRD, and Raman spectroscopy. In this study, we evaluated Sunset Yellow FCF (SY) dye removal as a model to understand bonding structures among magnetic HNTs, magnetic particles, and dye molecules. We focus on the interactions of SY-magnetic HNTs and characteristics of magnetization by VSM after SY dye adsorption, which highlight the notable features of magnetic halloysite nanotubes. We used different pH environments to study the behavior of magnetic HNTs after dye absorption. The application of these modified HNTs is promising for future organic dye removal and wastewater treatment.

* Corresponding author.
E-mail addresses: chemistquang95@gmail.com (N.Q. Nguyen), yheej@hanyang.ac.kr (Y. Jeong), L.Abelmann@tudelft.nl (L. Abelmann), junguryu@hanyang.ac.kr (J. Ryu), dsohn@hanyang.ac.kr (D. Sohn).

https://doi.org/10.1016/j.colsurfa.2023.132631
Received 21 September 2023; Received in revised form 15 October 2023; Accepted 20 October 2023
Available online 23 October 2023

1. Introduction

In the past decade, several industries have been widely using water-soluble acid dyes for food, cosmetics, and textiles. All dye compounds are pollutants or residues of organic mixtures and are probably harmful to all aqua cultures and humans [1]. Some organic dyes are not biodegradable due to the stable complexes of aromatic structures. The accumulation of high-concentration dyestuffs in an aqueous environment may cause serious problems of carcinogenicity and toxicity [2–4]. Thus, the increasing necessity of numerous techniques for water treatment is necessary, especially in the field of wastewater. To achieve dye removal, several chemical, physical, and biological methods have been developed including coagulation, chemical oxidation, degradation (electrochemical, photocatalytic, aerobic, and anaerobic microbial), membrane separation, and adsorption [5–11]. Among these methods, adsorption is a typical candidate due to its low cost, simple concept, and ease of implementation [12].

Mesoporous materials are a fascinating category of materials that possess unique properties such as high surface area, adjustable range of pore size (from 2 to 50 nm), and well-defined pore structures that allow their application in chemical sensing, adsorption, and photocatalysis [13–15]. However, using pure mesoporous elements like silica in wastewater treatment is not very effective due to their low thermal and hydrothermal stability. To overcome this, doping of heterogeneous atoms on the surface of native mesoporous material has become popular in water research [16]. Amorphous mesoporous structures play a significant role as a supporting material, but chemical modifications, such as doping with nanoparticles, can enhance their properties and result in synergistic effects in adsorption and photocatalysis.

Moreover, the adsorption method has been used for more than 100 years since first receiving attention in 1912 when Chapman and Siebold used kaolin clay mineral [17]. In nature, clay minerals are popular worldwide at a reasonable cost. Clay minerals provide great potential as effective and recyclable adsorbents and dye removers [18,19]. Specifically, inorganic clay minerals are ubiquitous due to their various morphologies including rod-like, fibrous, tubular, lamellar, and layer-pillared structures [20].

Among these inorganic clay minerals, halloysite nanotubes (HNTs) are eco-friendly adsorbents for many applications in green chemistry [21]. After the first mention in 1826 by Berthier as a clay mineral of the kaolin group with a 1:1 dioctahedral structure, the chemical formation of halloysite is slightly different in that its unit layers are separated by a water monolayer [22]. The formula of halloysite clay can be described as $Al_2Si_2O_5(OH)_4 \bullet nH2O$ [23]. Structurally, HNTs form an aluminosilicate mineral similar to kaolinite and are composed of a Si-O-Si tetrahedral sheet that is overlapped by an octahedral Al-OH group inner surface [24], [25].

Natural HNTs have a hollow interior, with a wall thickness that can vary between 10 and 50 nanometers. The inner and outer surfaces of HNTs, known as their lumens, are smooth and covered with hydroxyl groups, providing the material a negative charge. Halloysite nanotubes may provide a unique interpolating space with water molecules to provide a 10 Angstrom (Å) basal layer within the lumens [26]. The surface charges of HNTs make the system highly reactive, easily absorbing and retaining various molecules and ions.

Halloysite clay has garnered considerable attention from the scientific community due to its biocompatibility and low toxicity [27]. Creating a layer-by-layer structure in the confined tubular HNT lumen is important. In addition, attachment of magnetic nanoparticles to the surface of HNTs is crucial for the separation of modified magnetic HNTs in dye removal applications. This strategy provides a unique tubular porous structure and a large surface area typical of natural aluminosilicate clay mineral to provide high adsorption and high selectivity for many chemicals [28,29].

Acidification of the clay minerals can remove all the functional carbonate groups and metal ions that leach in the process, allowing enhanced adsorption properties of magnetic HNTs [30]. Acid treatment of clay minerals effectively can remove carbonates and partially remove metal ions. Acid treatment also results in an increase in the number of silanol groups, surface activity, and acidic sites, which ultimately improve the adsorption properties of clay minerals. Notably, the Si-O-Si bonds or silicate clay are not damaged by common acids other than hydrofluoric acid (HF) [31]. In contrast, alkaline conditions have been shown to possess stronger corrosion capabilities, affecting both metal cations and Si-O-Si bonds. Thus, in this research, three pH environments of pH 4, pH 7, and pH 10 are tested.

Several dyes have been investigated [32]. Among these, Sunset Yellow FCF was selected to test the ability of magnetic HNTs to separate and remove dyestuffs. The major features of Sunset Yellow FCF would be navigated by this work and other comparisons are mentioned in the supplementation with the other two dyes, which are Methylene Blue and Rhodamine B. Sunset Yellow FCF is a typical synthetic dye with five main characteristics suitable for this research. First, it is used in various industries, including textiles, cosmetics, and food coloring [33]. Second, this yellow dye is an aromatic compound with a fixed molecular weight of 432.4 g/mol, indicating that these molecules contain one or more aromatic rings in the chemical structure [34]. This common feature provides an intense and long-lasting color. Third, Sunset Yellow is highly soluble in aqueous solutions, especially water, allowing this dye to be easily utilized in many water-based environments [35]. Moreover, this yellow chemical has been reported to have some degree of toxicity, particularly at high concentrations [36]. Last, adsorption of Sunset Yellow FCF dye molecules in aqueous solutions can be achieved using positively charged surfaces [37]. Fig. 1.

2. Materials and methods

2.1. Solvents and reagents

Halloysite nanotubes (HNT, kaolin, molecular weight (MW) = 294.19 g/mol; CAS No.: 1332–58–7) and Sunset Yellow FCF Dye content 90% (452.37 g/mol; d = 0.617 g/cm^3; CAS No.: 2783–94–0) were purchased from Sigma Aldrich. $FeCl_2 \bullet 4\ H_2O$ (d = 2.53 g/cm^3), $FeCl_3 \bullet 6\ H_2O$ (d = 1.82 g/cm^3), and ethanol (Absolute, MW = 46.07 g/mol; CAS No.: 64–17–5) were purchased from Merck Millipore. Deionized (DI) water was extracted from Milli-Q (Perm C =11.3 μS/cm; resistivity = 18.2 MΩ•cm). Sodium hexaphosphate (SHMP) and other chemical reagents were purchased from Sigma Aldrich.

2.2. Halloysite nanotube purification

Briefly, 25 g of halloysite nanotube clays were placed in a two-neck, round Duran glass flask and dissolved in 125 mL DI water with a cross magnetic bar constantly stirring for 3 h. Then, 2.5 g of SHMP $(NaPO_3)_6$, granular, > 99%, Alfa Aesar) was added to the mixture under constant stirring while the pH of the solution was modified to 8.5 using 0.1 M NaOH aqueous stock solution (98%, GR, Daejung Chemicals). Next, the obtained mixture, including the purified HNTs, was decanted and centrifuged at a rotational speed of 2500 revolutions per minute (rpm) for 12 min. The precipitates were washed with DI water several times and combined with the sedimentation phases until the supernatant of the washed solution was clear before another centrifugation process at 10,000 rpm for 15 min. The obtained precipitate was dehydrated via lyophilization for 2 days to remove any water traces and droplets in the centrifuge tubes. The final dried powder was denoted as 'pHNTs,' pristine HNTs.

2.3. Modification of magnetic halloysite nanotubes

Synthesis of mHNTs from the obtained pHNTs is described in a previous study [38]. Briefly, the pHNTs were preheated in an oven at 100 °C for 12 h. Next, 0.5 g of preheated pHNTs dissolved in 150 mL DI

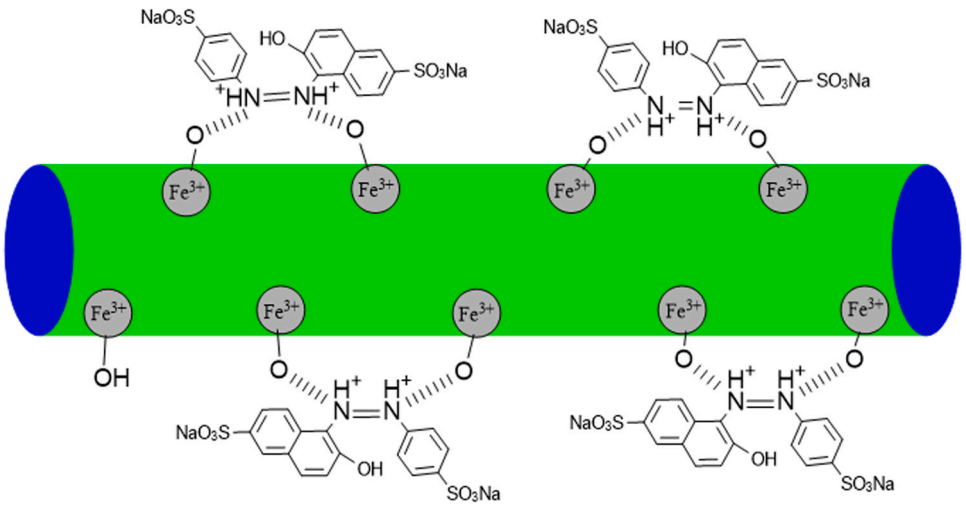

Fig. 1. The structure of modified magnetic halloysite nanotubes with Sunset Yellow FCF dye molecules.

water in a two-neck, round Duran glass flask were sonicated for 15 min under N_2 purging and stirring. Afterward, 1.3 g of iron (III) chloride hexahydrate ($FeCl_3$•6 H_2O) and 0.48 g of iron (II) chloride tetrahydrate ($FeCl_2$•4 H_2O) were gradually added to the mixture with constant stirring for 15 min at 60 °C (immersed in an oil bath to control system temperature). Then, 10.00 mL of ammonium water (CAS No.: 1336–21–6) was added dropwise to the solution at the rate of 0.05 mL/minute with the use of a syringe pump and a 10.00 mL Henke-Ject syringe connected to a septum of the flask. The reaction was conducted for 8 h in an oil bath at 70 °C to obtain a black slurry mixture containing magnetic HNTs. The slurry solution was washed three to four times sequentially with a mixture of DI water and anhydrous ethyl alcohol 99.9% (CAS No.: 64–17–5) at a ratio of 1:2. The obtained mixture was dried in an oven overnight at 65 °C.

2.4. Dye absorption process

The dyes are herein labeled 'MB' for Methylene Blue, 'RB' for Rhodamine B, and 'SY' for Sunset Yellow. Samples of magnetic HNTs with dye mixtures are designated as MBB, RBB, and SYB before the experiment, standing for Methylene Blue Before, Rhodamine B Before, and Sunset Yellow Before, respectively. After the dye experiment, the remaining samples in the dye stock solution are designated MBA -Methylene Blue After, RBA-Rhodamine B After, and SYA-Sunset Yellow After.

The powders of SYB-mHNTs were prepared in the same small amounts and were dissolved in solutions with similar pH conditions. A similar method was applied to all the vials containing magnetic HNTs. However, the SYA-mHNTs were separated with various methods after the dye removal experiment. The mixtures of colorless solutions and magnetic HNTs in dye vials were lyophilized overnight to remove all water. In this study, modified magnetic HNTs were synthesized for Sunset Yellow FCF recognition, and the solution pH was 4, 7, or 10. At these pH values, magnetic HNTs were shown to be promising candidates in several facile adsorption-desorption processes for dye removal and water treatment.

2.5. Characterization techniques

2.5.1. Scanning electron microscopy (SEM)

A surface morphology study was conducted via scanning electron microscopy (SEM) experiments by analyzing the layers of all specimens. Specifically, the specimens were loaded onto a silicon wafer square (7 mm × 7 mm) using 2–3 droplets of each sample solution and were dried overnight at room temperature. A thin layer of gold was coated onto the surface of each specimen in 120 s by the ion-sputtering coater MCM-200. Halloysite nanotubes are non-conductive samples, and the use of an ion-sputtering coater prevents electron charging during electron beam imaging. In addition, this method also produces high conductivity of the specimens and improves imaging resolution, sharpness, and magnification. Samples of pristine halloysite nanotubes, magnetic halloysite nanotubes, and mHNTs before and after dye removal were observed using a field-emission scanning electron microscope (FE-SEM, ThermoFisher APREO S HiVac, FEI) in a high-vacuum environment. The acceleration voltage for FE-SEM characterization was 15.00 kV, and secondary electrons and back-scattered electrons were simultaneously detected.

2.5.2. Transmission electron microscopy (TEM)

The transmission microscopic morphology of magnetic halloysite nanotubes was optimized on a JEOL JEM-2100 F with a microscope energy system at 200.00 kV. The single-tile specimen holder was EM-21010/21020, and the TEM images were captured individually at high current, and the auto emission current ranged from 13.9 μA to 94.9 μA.

2.5.3. Energy dispersive X-ray spectroscopy (EDS)

The following EDS characterization by TEM on a JEM-ARM200F (HRP) instrument comprised acquisition parameters of a probe current of 7.475 nA, a scan time of 180 s, and a counting rate of 340–600 cps in the energy range of 0–40 keV.

2.5.4. X-ray photoelectron spectroscopy (XPS)

XPS measurements were conducted on a K-Alpha$^+$ Spectrometer System (Thermo Scientific, USA) with a micro-focused monochromatic Al K_α X-ray source of 1486.6 eV. The equipment method used was a survey scan with a range of 0–1400 eV, and all core-level spectra were referenced to the $C_{1\,s}$ hydrocarbon peak at 285.0 eV. All the pHNTs, mHNTs, and dye solutions before and after dye removal were dried and cast onto a 10 mm × 10 mm silicon wafer. They were mounted inside the analysis chamber on a 60 mm × 60 mm stage to allow variation in the position of the electron beam, and the energy input was 12 KeV/6 mA.

2.5.5. X-ray diffraction (XRD)

X-ray diffraction was conducted using a Bruker D8 ADVANCE diffractometer for real-time component recognition and validation using a coupled (θ)/theta scan. The analysis angle was 5–90° (step: 0.02°), and the scan speed time [time/step] was 0.4 s

2.5.6. Fourier transform – infrared (FT-IR) spectroscopy

The FT-IR measurement of the sample was conducted using a Thermo Scientific Nicolet iS50 spectrometer with step-scans to compare the mHNTs after Sunset Yellow FCF dye absorption in three pH conditions.

2.5.7. Raman spectroscopy

Raman spectroscopy measurements were performed with a dispersive Raman microscope equipped with a PhAT probe providing a laser beam source ($\lambda = 785$ nm, power: 40 mW), illumination diameter of 1 mm, and a CCD detector (Kaiser Optical Inc., USA).

2.5.8. Vibrating sample magnetometer (VSM)

To prepare samples for vibrating sample magnetometry, an amount of sample with 3–7 mg of powder was entered with a spatula into 2 mL Eppendorf tubes and weighed. Demineralized water was added to achieve a concentration of 2.0 ± 0.1 mg/mL. After ultrasonic agitation, a 20 μL droplet was carefully deposited on an 8 mm × 8 mm silicon substrate and left to dry overnight.

The in-plane magnetic hysteresis loops of the dried deposits on the silicon substrates were measured with a DMS model 10 vector VSM. The system was calibrated with a 0.3 mm thick Ni foil of 6 mm diameter, which is approximately the size of the dried droplet. The disc has a weight of 70.6 mg which assumes a moment of 3.89 mAm^2 using the literature value for the saturation magnetization of Ni (55.1 Am^2kg^{-1}) [39]. The diamagnetic contribution of the sample holder and the Si substrate was subtracted by a linear background signal of 0.5 μAm^2T^{-1}, obtained by a fit to the high field branches of the in-plane hysteresis loops. The hysteresis loops were taken at the maximum field range of 2 T, to ensure the samples were saturated.

This study analyzed the reproducibility of the sample preparation method on pure Fe_2O_3 and Fe_3O_4 powder. Despite efforts to weight and transport accurately, the variation in saturation magnetic moment was as high as 70%. For a more accurate determination of the saturation magnetization, larger quantities are required. We could however not increase the deposited volume over 20 μL without overflowing the substrate.

2.5.9. Brunauer-Emmett-Teller (BET) measurement

The pretreatment of mHNTs and SYA-mHNTs before BET measurement includes several steps. Both sample types were kept in a vacuum oven at 180°C for 3 h, and then the weight was measured before pretreatment. Samples were measured using Helium as the gas carrier and N_2 as the exchange gas on a BELSORP-Mini II (BEL JAPAN Inc.). A standard sample cell of ~ 1.8 cm^3 contains 0.3 g of the sample after pretreatment for BET characterization.

3. Results and discussion

3.1. SEM characterization

SEM was used to characterize the structures and sizes of the pHNTs after purification and was used to characterize the mHNTs after modification of the magnetic particles. The morphologies of pHNTs (Fig. 2A) and mHNTs (Fig. 2B) illustrate the significant differences after synthesis and modification of magnetic particles to pHNTs. Fig. 2B reveals that the mHNTs contained many clusters of a combination of magnetic nanoparticles and modified halloysite nanotubes. From this, we concluded that mHNTs formed in sizes up to approximately 2 μm in length, which are larger than the uniform purified pristine HNTs of 500 nm in length. Figs. 2C to 2E show that the diameter of the mHNTs was approximately 30 nm in acidic conditions and larger in NaOH solution. Micrographs of materials at pH 4, pH 7, and pH 10 show the distribution and surface of magnetic HNTs in different environments. Different roughnesses on the surface are shown in Figs. 2C and 2E. However, the system for mHNTs-SYA in pH 4 showed distributed crystallized clusters of magnetic particles with HNTs, different from the other environments. Magnetic particles in mHNTs-SYA 10 are shown in Fig. 2E, while the blended system of mHNTs-SYA 7 in Fig. 2D is more densely packed and has a complex morphology.

The consistency of halloysite nanotubes after dye absorption is unchanged in morphology at pH 7 as the provided supplement information data (Figure SI 1). However, the size of the magnetic particles on the surface of HNT outer lumens are extensively different in terms of SYA in comparison with MBA and RBA. Specifically, the absorbed magnetic nanoparticle size is in the range of 17.00–22.70 nm for MBA (Figure SI 1 A), and 17.05–21.13 nm for RBA (Figure SI 1B) respectively while the one in SYA is from ~26.00–42.68 nm (Figure SI 1 C) approximately. It confirms that the dye molecules are attached to the magnetic particles on the outer surface of the HNT lumens. This characteristic of outer

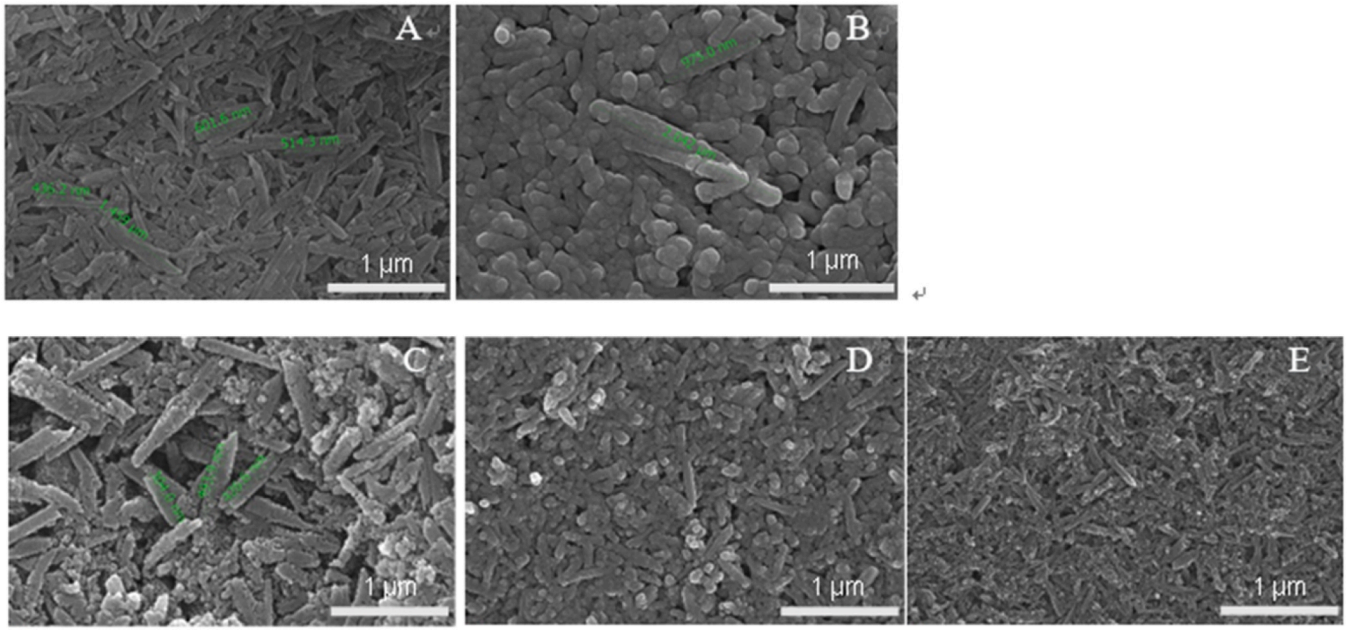

Fig. 2. SEM images of (A) pristine HNTs-pHNTs, (B) magnetic HNTs-mHNTs, (C) mHNTs in pH 4, (D) mHNTs in pH 7, and (E) mHNTs in pH 10.

surface adsorption for magnetic HNTs would be clearly analyzed and supported in TEM and EDS characterization.

3.2. TEM characterization

Representative TEM images of the pHNT indicated that pristine halloysite nanotubes provided an inner lumen < 15 nm and an outer lumen < 50 nm after purification (Fig. 3A). On the other hand, magnetic particles on the surface of the mHNTs varied in behavior in different environments of pH 4 in CH_3COOH (Fig. 3B), pH 7 in a mixture of water and ethanol (Fig. 3C), and pH 10 in NaOH (Fig. 3D). According to TEM, magnetic HNTs in CH_3COOH and in NaOH were slightly different in magnetic particle size and lumen diameter. Specifically, the inner lumen diameter is 12.69 nm and 40.94 nm respectively in acid and basic condition of mHNTs while the particles in both environments are mostly unchanged with diameters of 12.66–17.90 nm in CH_3COOH and 12.78–19.13 nm in NaOH. Thus, the lumen diameter remained unchanged in acidic conditions but were smaller than those in basic conditions in which the particles seem to increase in size. Nanoclusters consisting of magnetite nanoparticles as subunits were also observed on the surface and inside of mHNTs at pH 7 and pH 10, respectively.

After the absorption of Sunset Yellow FCF dye, a TEM morphology analysis was carried out to investigate the structure of mHNTs (Figs. 3E and 3F). The results showed that some magnetic nanoparticles adhered to the walls of the hollow cavities of HNTs. This finding could be attributed to the unique structure of HNTs, which have a large surface area, large pore volume, and adequate hydroxyl groups that make it easier for metal ions to access and adsorb onto the surface. The large surface area of the HNTs provided more sites of adherence for the magnetic nanoparticles, while the large pore volume allows greater access to the interior of the cavities. Additionally, the presence of hydroxyl groups on the surface of the HNTs make it easier for metal ions to adsorb onto the surface due to their affinity for hydroxyl groups. These findings provide promising insights into the structure and properties of mHNTs and could have potential applications in various fields including drug delivery, catalysis, and imaging.

An emphasis of comparison with other two dyes including Methylene Blue and Rhodamine B is demonstrated in the Supplementation Information 2 (Figure SI 2). It is obvious to demonstrate that all the magnetic nanoparticles attached to the surface of the outer HNTs lumen would expand in size. Also, several dye molecules are scavenging on the outer surface after dye absorption process according to Figure SI 1 A for Methylene Blue, Figure SI 2B for Rhodamine B and Figure SI 2 C for Sunset Yellow FCF.

3.3. EDS characterization

The analysis of EDS was characterized by scanning the main elements in the process of synthesizing magnetic halloysite nanotubes. In Fig. 4A, the presence of aluminum, silicon, carbon, oxygen, nitrogen, and iron in the mHNTs system was confirmed at appropriate counts per second (cps). Moreover, the contribution of iron in EDS characterization was 5.3%. The backscattering EDS images in Fig. 4B illustrate the element distribution in a region of a single magnetic halloysite nanotube. As can be seen from Fig. 4C, magnetic particles remained on both the outer and inner lumens of mHNTs.

Similarly, the percentage of Fe is exponentially decreasing to approximately less than 2% in the order of MBA > SYA > RBA with

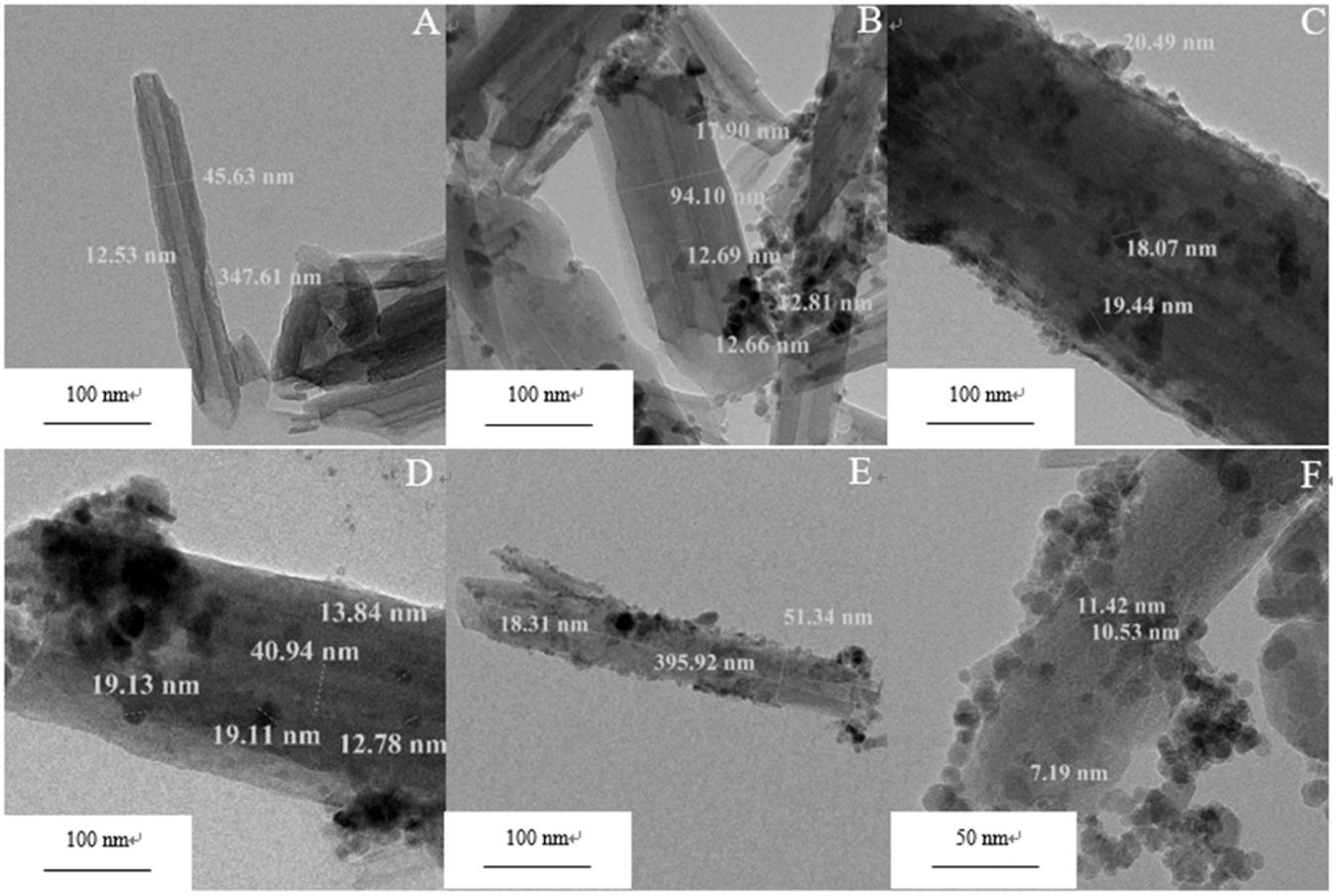

Fig. 3. Transmission electron spectroscopy of (A) pHNTs, (B) mHNTs in CH_3COOH, (C) mHNTs in DI water & ethanol mixture, (D) mHNTs in NaOH, (E) SYA-mHNTs (scale 100 nm), and (F) SYA-mHNTs (scale 50 nm).

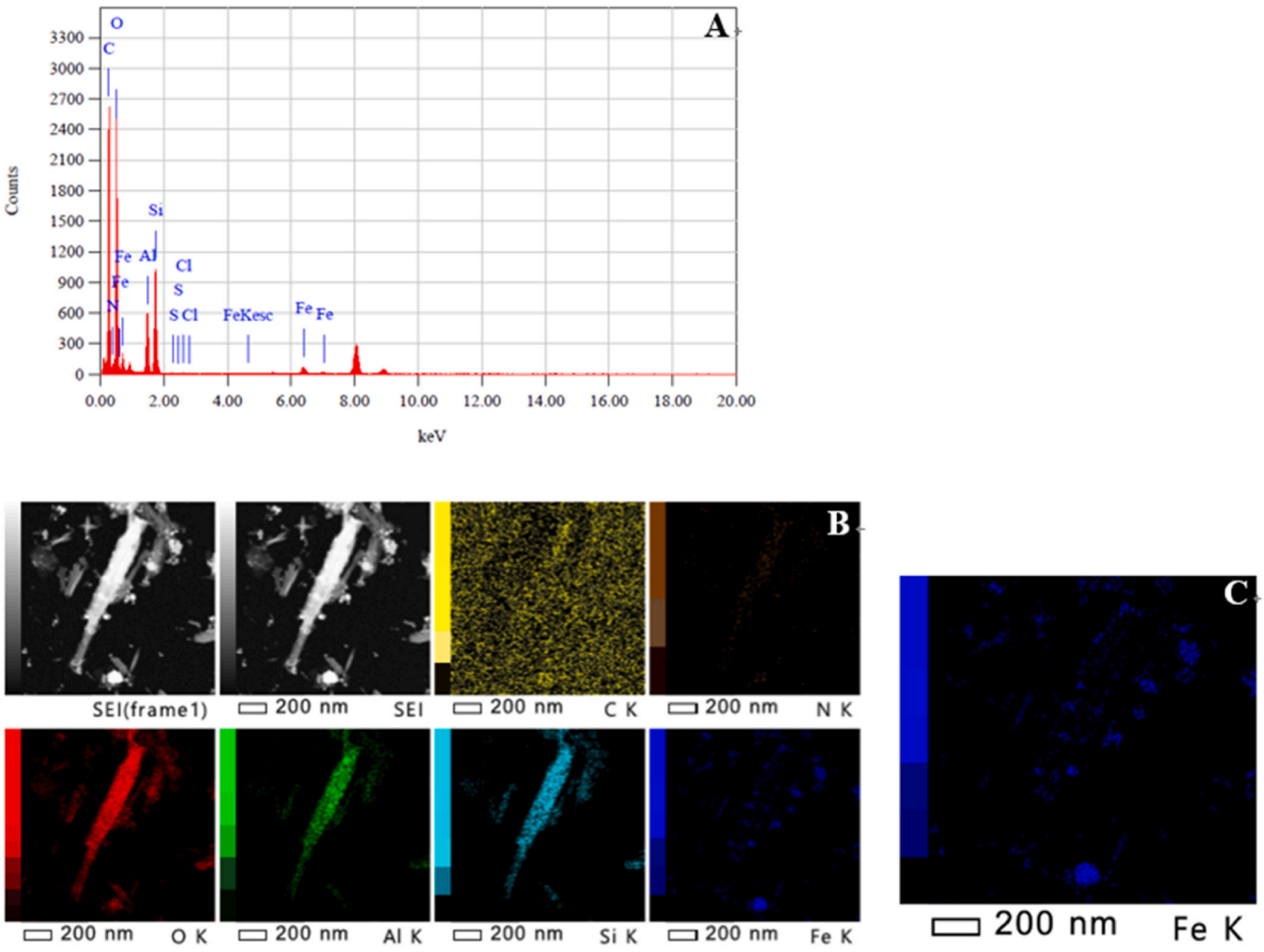

Fig. 4. (A) EDS measurement of magnetic halloysite nanotubes (keV), (B) backscattering element scan at 200 nm, and (C) Fe EDS scan at 200 nm.

1.89%, 0.44% and 0.29% after dye absorption process in accordance with the Figure SI 3 including Figure SI 3A Figure SI 3B and Figure SI 3C, respectively. This EDS results in the interaction between the dye molecules and magnetic particles on the outer lumen of magnetic halloysite nanotubes for decrease of Iron ratio in comparison with other elemental ratios remaining unchanged.

3.4. XPS characterization

X-ray photoelectron spectroscopy was used to compare pHNTs and mHNTs, and the magnetic halloysite nanotubes produced peaks of Fe_{2p} at binding energies of 712 and 725 eV. The ratios of Al-Si in terms of magnetic and pristine halloysite were significantly different in the two graphs in Fig. 5. In terms of pHNTs, the Al-Si ratio fit with the natural background of purified pristine halloysite nanotubes, while Al_{2p} intensity in mHNTs was negligible due to the dominance of magnetic particles on the surface and inside the lumens of nanotubes. The proportion of Fe in mHNTs was 15% of elemental composition, and a small peak assigned to Cl_{2p} was indicated the involvement of ferric salt. The detailed assignment for the binding energy of other elements is listed in Table 1 for the sample of magnetic halloysite nanotubes. [40].

3.5. FT-IR spectroscopy analysis

Fourier transform infrared spectroscopy of the adsorption process was carried out before and after the interference of Sunset Yellow dye. The y-axis was transmittance in percentage (%), and the x-axis was wavelength in cm^{-1}.

FT-IR spectroscopy is commonly used to verify the formation of magnetic HNTs (Fig. 6B) and pristine HNTs (Fig. 6A) during the modification process. The sharp peaks at 893 cm^{-1} and 887 cm^{-1} correspond to the H-O-H deformation band in absorbed water. Peaks at 3675 cm^{-1} are the stretching of perpendicular surface -O-H, and that at 3601–3605 cm^{-1} is -O-H stretching of inner hydroxyls. The peaks at 1614 cm^{-1} and 1616 cm^{-1} for mHNTs and pHNTs, respectively, are bending of -OH in absorbed water. This bending allows the inner lumen of mHNTs to expand, producing peaks at 893 and 991 cm^{-1} for pHNTs and at 887 and 987 cm^{-1} for mHNTs. The moderate peak at 732 cm^{-1} identified the symmetric stretching of Si-O, and the peak around 618 cm^{-1} represents the presence of Fe_3O_4 in mHNTs. Uniquely, the peak at 2834–2900 cm^{-1} (associated with mHNTs) is due to symmetric C-H bonding, which is in a different area from those of pristine halloysite nanotubes.

3.6. UV-visible spectroscopy

The color change of Sunset Yellow FCF after adsorption was analyzed by a comparison with two other synthetic organic dyes at two concentrations of 0.01 M and 0.05 M. Fig. 7A and Fig. 7D show that the 0.01 M dye stock solution was nearly transparent, especially in terms of sunset yellow and methylene blue. By increasing the concentration by five times, as in Fig. 7B and Fig. 7E, the SY solution was transformed from an

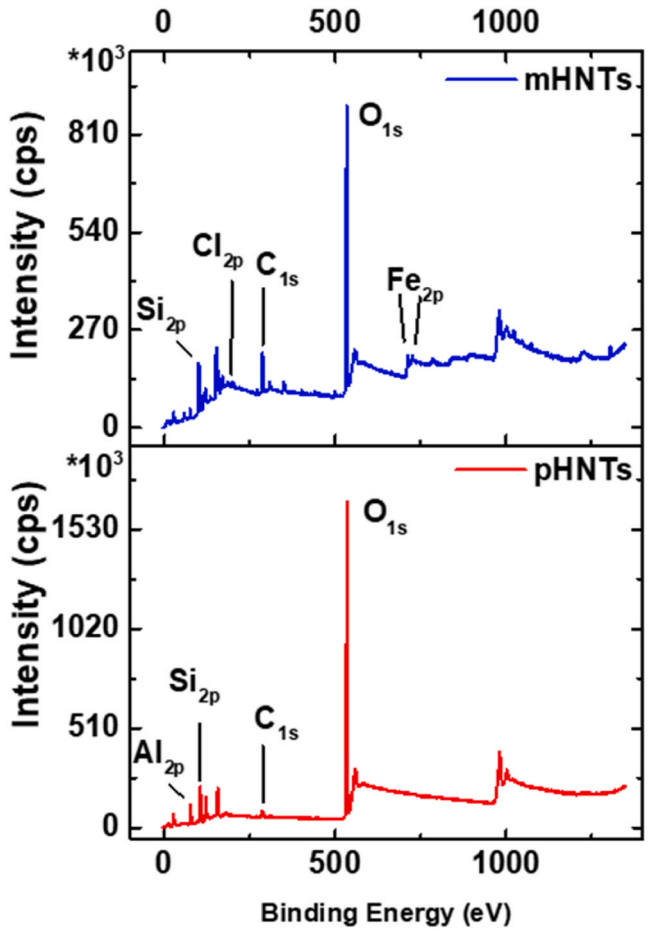

Fig. 5. XPS binding energy graphs of mHNTs (blue) and pHNTs (red).

Table 1
Binding energy summary for main elemental XPS analysis in mHNTs.

Element Name	Starting Binding Energy (eV)	Peak Binding Energy (eV)	Ending Binding Energy (eV)
Al_{2p}	79.73	75.92	72.49
Si_{2p}	107.35	104.05	100.23
Cl_{2p}	203.55	199.45	196.77
$C_{1\,s}$	293.07	285.55	282.52
$N_{1\,s}$	404.90	400.73	396.49
$O_{1\,s}$	537.32	533.10	528.16
Fe_{2p}	740.19	711.49	706.64

orange-yellow color before adsorption to a lighter yellow after adsorption. The added SY dye in Fig. 7C and Fig. 7F had a concentration of 0.01 M.

The absorption ability of magnetic halloysite nanotubes was described via UV–vis study of SYB and SYA, as shown in Fig. 8. At the beginning of the preparation phase, the intensities of the characteristic peaks of SY (255 nm, 310 nm, and 480 nm) were in the order of SYB4 < SYB7 < SYB10. When mHNTs were used for the sunset yellow system, all the characteristic peaks tended to behave in different orders. First, the peak of 255 nm broadened, while the 480 nm peak significantly decreased, maintaining the adsorption level order of SYA10 < SYA4 < SYA7. On the other hand, the 310 nm peak almost disappeared in all three pH environments, indicating loss of the group as the absorbance increased.

According to the stock solution UV–vis spectroscopy from Fig. 9A, the identical main peak absorption of Methylene Blue, Rhodamine B and

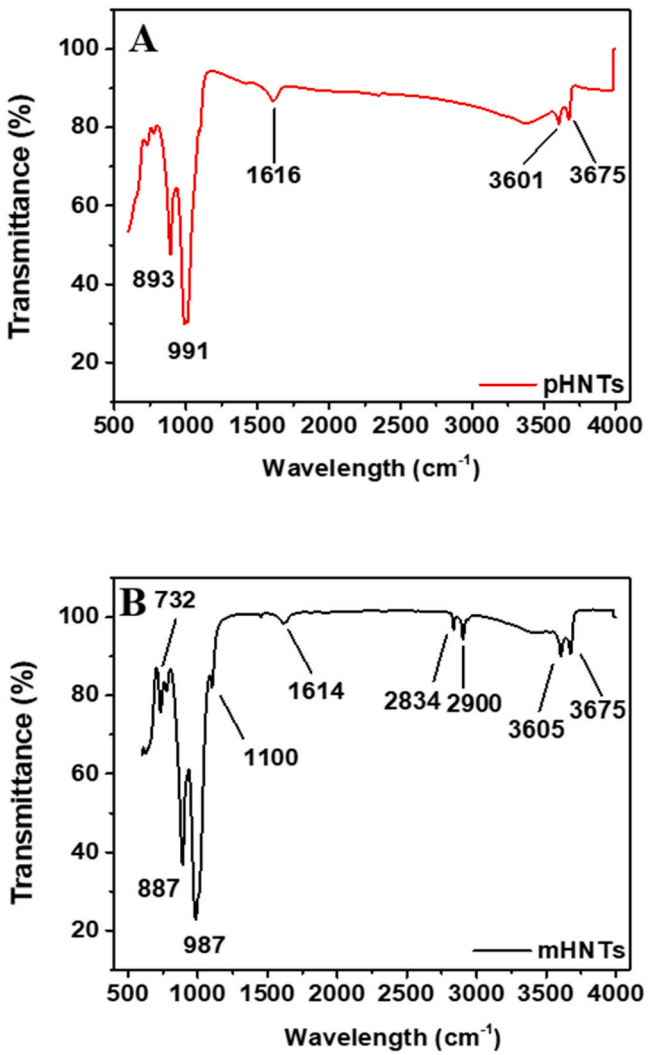

Fig. 6. Fourier transform infrared spectroscopy results of (A) pristine halloysite nanotubes and (B) magnetic halloysite nanotubes.

Sunset Yellow FCF are 665 nm, 555 nm, and 485 nm respectively. As a result of dye experiment comparison between the immersion of Fe_3O_4 (Fig. 9B) and mHNTs (Fig. 9C) at the mild pH conditions, the enhancement of dye discoloration in mHNTs is observed obviously in MBA-mHNTs for approximately 100% and SYA-HNTs for more than 85% while. The slight pink color of Rhodamine B makes the absorbance remaining at 0.3–0.4 a.u. surrounding the peak at $\lambda = 555$ nm. Hence, the adsorption capability of the dyes follows the order of MBA > SYA > RBA at pH 7.

3.7. Raman spectroscopy analysis

Raman spectroscopy was key to identifying, detecting, and quantifying the dye absorption capacity of magnetic halloysite nanotube before and after the process. The theory of polarizability by Placzek [39] was used to show that the spectral intensity of Raman bands differed by several orders of magnitude in each sample of mHNTs before and after dye absorption. As can be seen from Fig. 10A, more than 90% of the absorption peak were negligible and disappeared after immersion of mHNTs in sunset yellow solution. This means mHNTs effectively absorbed sunset yellow at pH 4. At pH 7, magnetic halloysite nanotubes also exhibited high adsorption efficiency, with the presence of all absorption peaks before and after the interference of Sunset Yellow FCF, as in Fig. 10B. Moreover, the dye absorption at pH 10 in NaOH provided

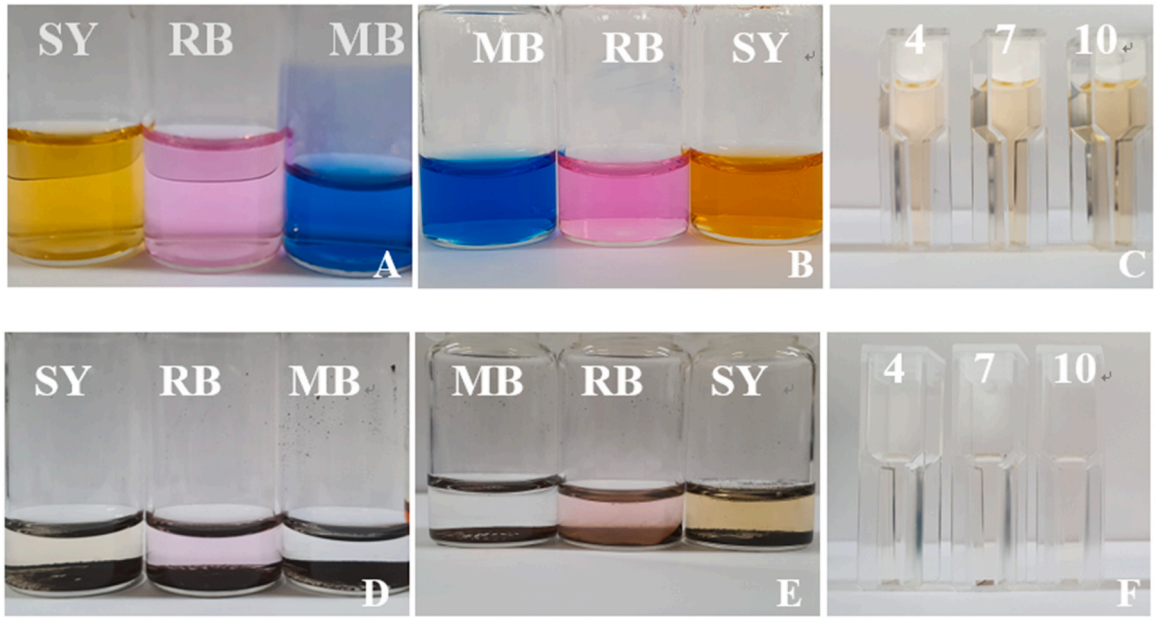

Fig. 7. (A) Dye stock solution 0.01 M; (B) dye stock solution 0.05 M; (C) 2.5 mL SYB solution 0.01 M at pH 4, pH 7, and pH 10; (D) SYA, RBA, and MBA 0.01 M; (E) SYA, RBA, MBA and 0.05 M; and (F) 2.5 mL SYA solution 0.01 M at pH 4, pH 7, and pH 10.

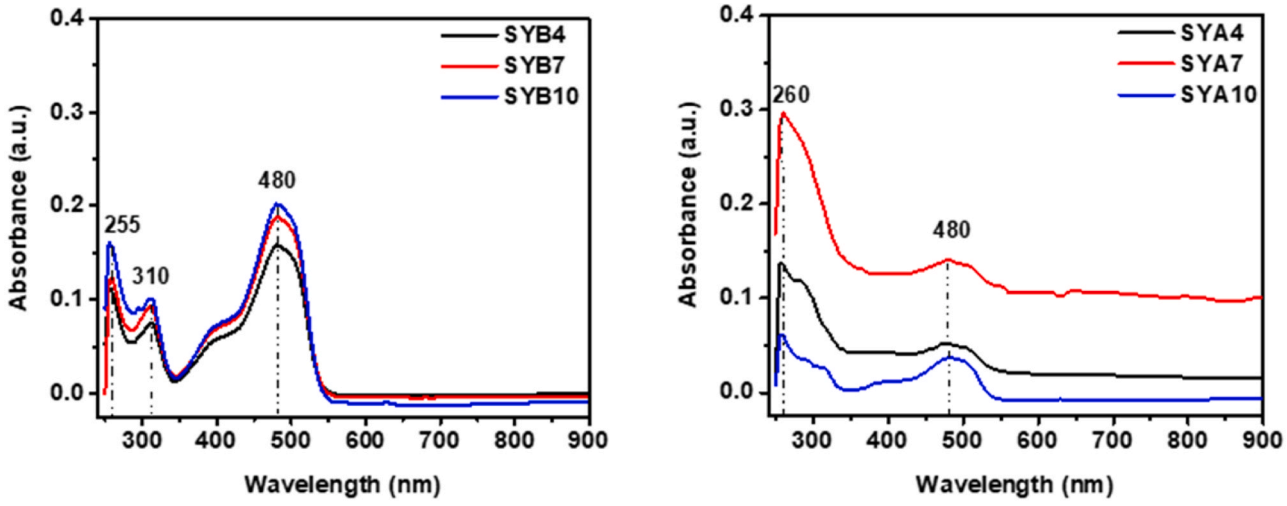

Fig. 8. UV–vis spectroscopy results of 0.05 M SYB (A) and SYA (B) at pH 4, pH 7, and pH 10.

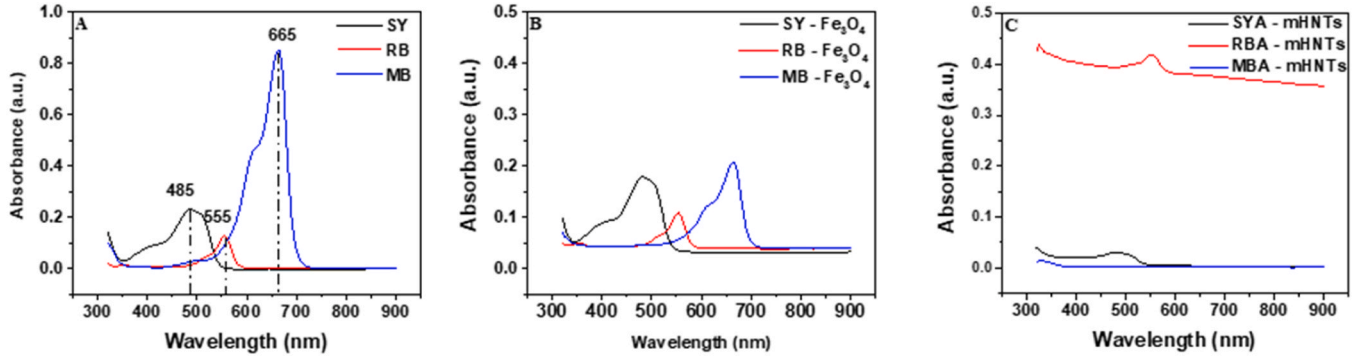

Fig. 9. UV–vis spectroscopy of (A) 0.01 M stock solution of SY, RB and MB dye, (B) Dye solution with Fe_3O_4 at pH 7 and (C) dye solution with mHNTs at pH 7.

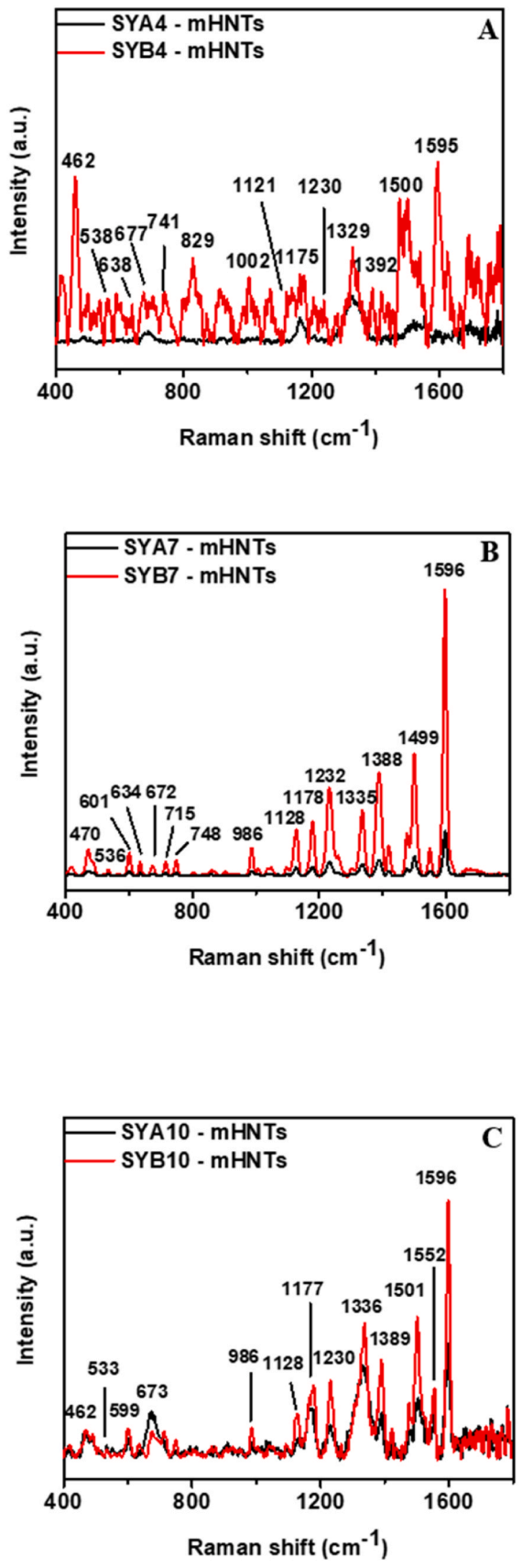

Fig. 10. Raman spectroscopy results of (A) SYB4-mHNTs and SYA4-mHNTs, (B) SYB7-mHNTs and SYA7-mHNTs, (C) SYB10-mHNTs and SYA10-mHNTs.

the lowest efficiency compared with other pH conditions in that most of the peaks decreased by several orders of magnitude but remained observable.

Evaluating the magnetic bonding transition before and after addition of sunset yellow dye is important and was conducted here using Raman spectroscopy as summarized in Table 2. Three main critical peaks for the bonding of Fe-C and for quantifying the structural system of magnetic halloysite nanotubes and dye molecules produced vibration peaks at 462–470 cm^{-1} for Fe-C bonds and at 533–538 cm^{-1} and 672–677 cm^{-1} for magnetite Fe_3O_4 [41]. The absorption peak of N = N stretching in the region 1121–1128 cm^{-1} was not observed after the addition of Sunset Yellow due to the functional bonding between dye molecules and magnetic particles.

The comparison of the molecular interactions between magnetic halloysite nanotubes before and after dye adsorption of among (A) MBB4-mHNTs and MBA4-mHNTs, (B) MBB7-mHNTs and MBA7-mHNTs, (C) MBB10-mHNTs and MBA10-mHNTs is illustrated in Figure SI 4. The summary of bonding assignments for Raman peak positions in terms of Methylene Blue is mentioned in Supplementary Information 5 (Table SI 5). After the Methylene Blue dye absorption by mHNTs, the main characteristic peaks of Fe-C shift several wavenumbers to the range 448–454 cm^{-1} while the peaks at 675–678 cm^{-1} are unchanged for Fe_3O_4 band assignment.

3.8. Zeta potential analysis

A Zetasizer Nano ZS was used to characterize the zeta potential in a liquid medium at different pH values for (a) pHNT and (b) mHNT. Zeta potential measurements were used to determine the high-performance characteristics of the medium, making them suitable for further experiments. The preparation phase included a suitable number of disposable folded capillary cells from Malvern Co. Ltd.

Zeta potential results (Fig. 11) demonstrate the charging behavior of magnetic and pristine halloysite nanotubes in different environments. Under a wide range of pH values, zeta potential affected the ability of the magnetic and pristine halloysite nanotubes to disperse uniformly in liquid medium. Compared to pHNTs, mHNTs showed better dispersion, especially at pH 7 (−30 mV), with strong repulsion for negatively charged particles of overall zeta potential and preventing agglomeration. During acid leaching caused by changing pH, protonation of the luminol Al-OH species on the surface of pHNTs occurred via H^+ ions present in the acetic acid solution, resulting in the formation of positively charged $[Al(OH)_2]^+$ species [42]. The subsequent weakening of bonds between Al and O atoms led to partial leaching of Al from halloysite nanotubes. This process decreased the Al content of each

Table 2
Bonding assignments of peak positions from Raman spectroscopy of SYA-mHNTs at pH 4, pH 7, and pH 10 (ρ = rocking; ν = stretching; and δ = bending).

SYA4 – mHNTs (cm^{-1})	SYA7 – mHNTs (cm^{-1})	SYA10 – mHNTs (cm^{-1})	Bond Assignment
462	470	462	Fe-C
538	536	533	Fe_3O_4
638	634	599	SO_3-R_2
677	672	673	Fe_3O_4
741	748	-	ρ(R_1)
829	-	-	ρ(N-N)
1002	986	986	C-H-R_2
1121	1128	1128	ν(N = N); (C-H- R_1)
1175	1178	1177	ν(N = N); ρ(C-H-R_1); ρ(R_1)
1230	1232	1230	δ(C-C-R_1); ν(C-N); ν(C-H-R_1)
1329	1335	1336	ν(C-N); ν(H-C-C-H-R_1)
1392	1388	1389	ν(C-C-R_2); δ(R_1, R_2)
1500	1499	1501	ν(C-N); ν(C-O); ρ(N-H)
-	1550	1552	δ(C-C-R_2); ρ(N-H); ρ(C-H)
1595	1596	1596	C-C-R_1; C-H-R_1

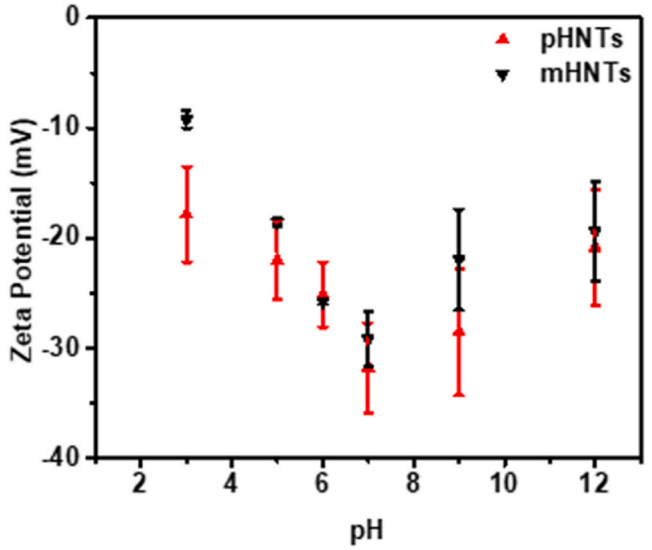

Fig. 11. Zeta potentials of pHNTs (red) and mHNTs (black) in the range of pH 3–12.

aluminosilicate layer from the inner shell to the outer shell, expanding the multi-layer structure within the nanotube lumen. Furthermore, the mean standard error of mHNTs was lower than that of pHNTs, showing a decrease in fluctuation in potential shift of mHNTs after scavenging of magnetic particles on the surface of the HNTs.

3.9. XRD analysis

X-ray diffraction is another crucial method for understanding the interaction of dye molecules and magnetic particles based on the synthesis and purification of pristine halloysite nanotubes. The X-ray diffraction results revealed the interactions between dye molecules and magnetic particles. As can be seen in Fig. 12, the mHNTs displayed distinct peaks compared to the pHNTs in the XRD spectra and demonstrated hematite nanoparticles according to JCPDS #01–075–0449. Additionally, the absorption of sunset yellow FCF demonstrated in the XRD pattern of mHNTs after dye absorption of Sunset Yellow illustrates SYA-mHNTs in the dried state in DI water. The 2θ values of the peak for magnetic particles were 30.1° and 43.1°, which are attributed to (220) and (400) crystal planes, respectively [43].

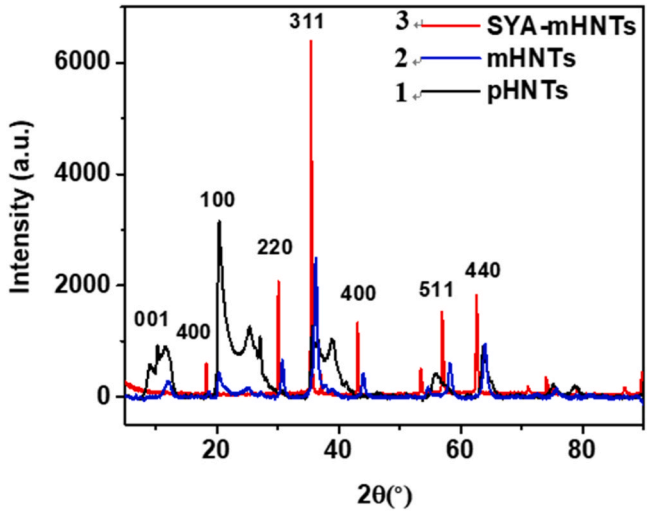

Fig. 12. XRD analysis of the pristine halloysite nanotubes (1), magnetic halloysite nanotubes (2), and SYA-mHNTs after SY dye absorption (3).

The (100) (h,k,l) values for the diffraction peak of the dehydrated state showed a d-spacing of 0.44 nm in pHNTs, which were lowest after modification of magnetic particles and were not observed after dye absorption. Following the absorption process, the SYA-mHNT sample exhibited high intensity with clear and sharp diffraction peaks. These peaks corresponded to the planes of the crystal structure, including (311), (511), and (440), which are associated with the cubic inverse spinel structure Fe_3O_4. These findings confirmed the anchoring of magnetic nanoparticles onto the surface of HNTs. Furthermore, these diffraction peaks tended to move 1–2 degrees to the left due to the bonding length and the variation with modification magnitude. After purification, the region of pHNTs at 7–12° remained broad, and a similar trend was observed in the presence of amorphous silica but was not observed after the synthesis and modification of magnetic particles and dye molecules according to the dealumination in the 2θ° region of 20–25° [44]. The large decrease in this region was due to dealumination after modification with the dye-magnetic particle system for SYA-mHNTs associated with partial loss of crystallinity after the synthesis of magnetic halloysite nanotubes for mHNTs.

3.10. BET analysis

The analysis of BET isotherms was used to understand the adsorption capacity of modified magnetic halloysite in the dye adsorption process before and after sunset yellow involvement.

In Fig. 12, the isotherm describes a similarity in N_2 adsorption of mHNTs before and after the interference of sunset yellow dye. Both graphs demonstrate the classification of Type IV isotherm by the International Union of Pure and Applied Chemistry (IUPAC), indicating the mesoporosity of magnetic halloysite nanotubes in the range of 2–50 nm. However, the monolayer-multilayer adsorption and capillary condensation showed a slight difference between the two samples. mHNTs (Fig. 13A) showed an H4 type hysteresis loop compared to SYA-mHNTs (Fig. 13B) with a small pore size distribution of an H3 type hysteresis loop. SYA-mHNTs provided a very narrow distribution, which means the sunset yellow dye molecules were adsorbed into the magnetic halloysite nanotubes with high efficiency. The capillary condensation phase of the SYA-mHNTs showed a p/p_{0-1} closer than that of mHNTs, illustrating high adsorption capacity of the non-rigid aggregates of plate-like particles.

3.11. Vibrating sample magnetometer

Fig. 14 shows the in-plane magnetic hysteresis loops of three samples taken from a basic (pH 10), neutral (pH 7) and acidic environment (pH 4). The shape of the hysteresis loops is not noticeably affected by the change in acidity. Since the sample preparation method suffers from inaccuracy, we chose to present the magnetic signal normalized to the saturation value. Table 2 shows the quantitative values for the coercivity and the susceptibility (the slope of the curve at $m/m_s = 0$). Both values, which are not dependent on the actual value of the saturation magnetization, are identical within measurement uncertainty with respect to acidity. Also, the variation in saturation magnetization is within the measurement uncertainty, which however is relatively large. Table 3.

According to the Stoner-Wohlfarth theory [45], the saturation magnetization M_s is in the region of 3–5 Am^2/kg and the coercivity is in the region of 2.0 ~ 2.4 mTesla with insignificant fluctuation recorded and summarized in Table 2. Hence, the process of mHNTs dye absorption does not affect the changes in saturation magnetization and other properties including susceptibility (S) and saturation magnetic moment (m) with negligible variation.

On the other hand, the modified magnetic HNTs illustrate the magnetic moment (m) at 0.553 nAm^2 for the beginning of the dye absorption (Figure SI 6B) as compared to 0.706 nAm^2 for pure Fe_3O_4 (Figure SI 6A). Approximately two cycles of mHNTs in pH 4 (0.22 nAm^2) and pH 10 (0.21 nAm^2) could be conducted by using the external magnetic field

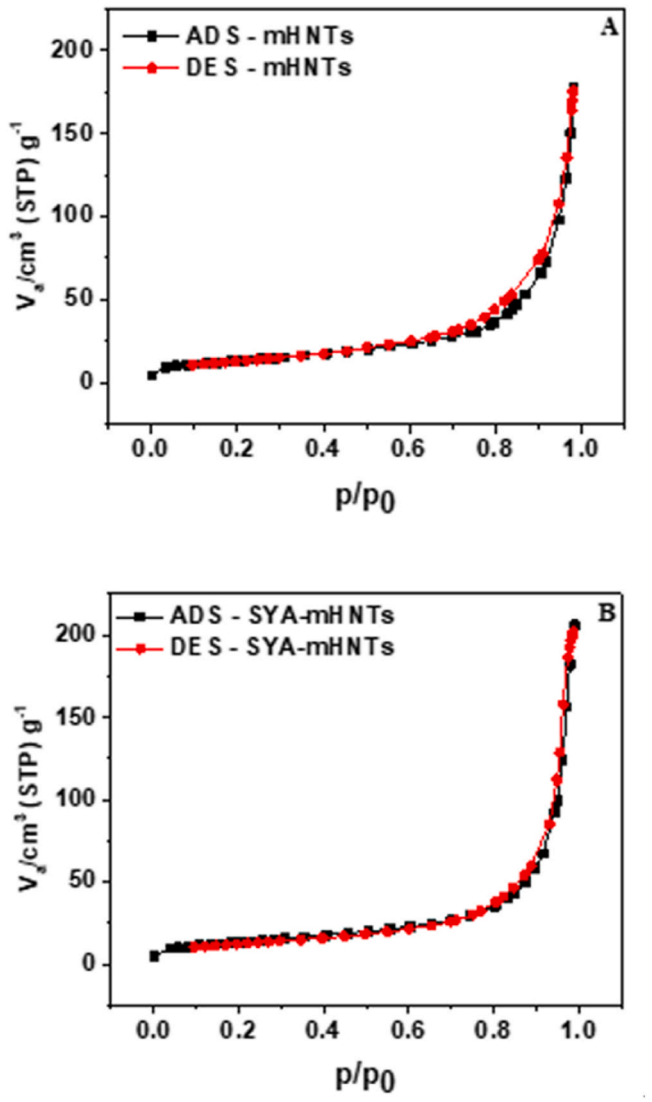

Fig. 13. (A) N_2 adsorption and desorption of mHNTs and (B) N_2 adsorption and desorption of SYA-mHNTs.

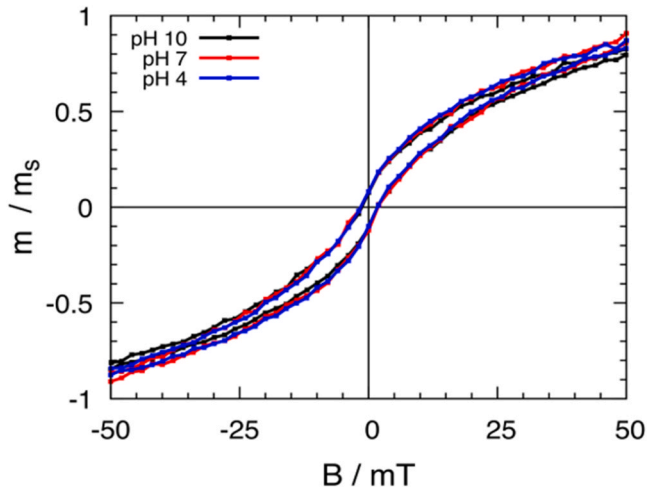

Fig. 14. Magnetic moment normalized to the saturation magnetic moment for samples that we exposed to a basic (pH 10), neutral (pH 7), and acidic environment (pH 4) after dye absorption.

Table 3
Saturation magnetic moment m, saturation magnetization M_s, coercivity B_c and susceptibility S at m = 0.

	m (nAm^2)	M_s (Am^2/kg)	B_c (mT)	S (1/T)
mHNT - pH 4	0.22 ± 0.08	5 ± 2	2.0 ± 0.3	35 ± 1
mHNT - pH 7	0.13 ± 0.04	3 ± 1	2.2 ± 0.2	35 ± 3
mHNT - pH 10	0.21 ± 0.08	5 ± 2	2.0 ± 0.4	37 ± 1

reusing for future absorption. In terms of pH 7, mHNTs described the highest efficiency with the magnetic nanoparticle and dye complexation showing the lowest magnetic moment and could be affected for the second cycle of reusing. The cycle of reusability for dye absorption depends on the ability of the magnetic field resulting in the attachment of magnetic particles on the outer surface of halloysite nanotubes. It is a promising characteristic for further in-depth analysis and investigation with the wide range of repeated VSM and dye absorption process.

4. Conclusion

Magnetic halloysite nanotube synthesis is environmentally friendly and suitable for further scaleup in industrial production at a reasonable cost. This nanomaterial has potential in various applications including colloids, dyes and pigments, absorbents, catalysis, and wastewater treatment. The analysis of bonding structures provided an understanding that can be used for further studies of interactions between magnetic halloysite nanotubes in several organic dyes with the main target of Sunset Yellow FCF in comparison with Methylene Blue and Rhodamine B. Different pH conditions influence magnetic halloysite nanotubes for future modifications and attachments for different uses. Among these, SYA-mHNTs at pH 7 demonstrate the highest adsorption capacity compared to those at pH 4 and pH 10. XPS was used to measure bonding energies between magnetic particles inside mHNTs, which are important in inorganic chemistry and surface catalysis. Moreover, the independence of BET analysis in the comparison is promising for use after incorporating magnetic nanoparticles onto the surface of halloysite nanotubes. Such magnetic halloysite nanotubes exhibited magnetic properties, which allowed them to be easily separated and recycled using a magnet. In conclusion, the magnetization effect is totally independence to the absorption capacity efficiency for the system of SYA-mHNTs. This magnetic functionality has the potential in applications in numerous fields, including catalytic reactions, adsorption, separation, and controlled drug release.

CRediT authorship contribution statement

The manuscript was written with the contributions of all authors. All authors have given approval to the final version of the manuscript. **Ngoc Quang Nguyen:** Conceptualization, Methodology, Writing - original draft, **Younhee Jeong:** Methodology, Writing - original draft, **Leon Abelmann:** Writing - review & editing, Data curation, **Jungju Ryu:** Writing - review & editing, **Daewon Sohn:** Supervision, Project administration, Funding acquisition, Writing - review & editing.

Declaration of Competing Interest

The authors declare that they have no known competing financial interests or personal relationships that could have appeared to influence the work reported in this paper.

Data availability

No data was used for the research described in the article.

Acknowledgment

This research was supported by the Basic Science Research Program administered through the National Research Foundation of Korea (NRF) and funded by the Ministry of Education (2020R1A6A1A06046728, 2022R1A2C1010580, and 2022R1A6C101A779–23).

Appendix A. Supporting information

Supplementary data associated with this article can be found in the online version at doi:10.1016/j.colsurfa.2023.132631.

References

[1] M.A.M. Salleh, D.K. Mahmoud, W.A.W.A. Karim, A. Idris, Cationic and anionic dye adsorption by agricultural solid wastes: a comprehensive review, Desalination 280 (1–3) (2011) 1–13, https://doi.org/10.1016/j.desal.2011.07.019.
[2] R. Al-Tohamy, S.S. Ali, F. Li, K.M. Okasha, Y.A.G. Mahmoud, T. Elsamahy, et al., A critical review on the treatment of dye-containing wastewater: Ecotoxicological and health concerns of textile dyes and possible remediation approaches for environmental safety, Ecotoxicol. Environ. Saf. 231 (2022), 113160, https://doi.org/10.1016/j.ecoenv.2021.113160.
[3] B. Lellis, C.Z. Fávaro-Polonio, J.A. Pamphile, J.C. Polonio, Effects of textile dyes on health and the environment and bioremediation potential of living organisms, Biotechnol. Res. Innov. 3 (2) (2019) 275–290, https://doi.org/10.1016/j.biori.2019.09.001.
[4] J. Sharma, S. Sharma, V. Soni, Classification and impact of synthetic textile dyes on aquatic flora: a review, Reg. Stud. Mar. Sci. 45 (2021), 101802, https://doi.org/10.1016/j.rsma.2021.101802.
[5] R.F. Gomes, A.C.N. de Azevedo, A.G. Pereira, E.C. Muniz, A.R. Fajardo, F. H. Rodrigues, Fast dye removal from water by starch-based nanocomposites, J. Colloid Interface Sci. 454 (2015) 200–209, https://doi.org/10.1016/j.jcis.2015.05.026.
[6] T. Cai, H. Li, R. Yang, Y. Wang, R. Li, H. Yang, et al., Efficient flocculation of an anionic dye from aqueous solutions using a cellulose-based flocculant, Cellulose 22 (2015) 1439–1449, https://doi.org/10.1007/s10570-015-0571-9.
[7] Q. Chen, P. Yu, W. Huang, S. Yu, M. Liu, C. Gao, High-flux composite hollow fiber nanofiltration membranes fabricated through layer-by-layer deposition of oppositely charged crosslinked polyelectrolytes for dye removal, J. Membr. Sci. 492 (2015) 312–321, https://doi.org/10.1016/j.memsci.2015.05.068.
[8] S. Wei, X. Hu, H. Liu, Q. Wang, C. He, Rapid degradation of Congo red by molecularly imprinted polypyrrole-coated magnetic TiO2 nanoparticles in dark at ambient conditions, J. Hazard. Mater. 294 (2015) 168–176, https://doi.org/10.1016/j.jhazmat.2015.03.067.
[9] X. Liu, Y. Yang, X. Shi, K. Li, Fast photocatalytic degradation of methylene blue dye using a low-power diode laser, J. Hazard. Mater. 283 (2015) 267–275, https://doi.org/10.1016/j.jhazmat.2014.09.031.
[10] Y.X. Liu, Z.Y. Liao, X.Y. Wu, C.J. Zhao, Y.X. Lei, D.B. Ji, Electrochemical degradation of methylene blue using electrodes of stainless steel net coated with single-walled carbon nanotubes, Desalin. Water Treat. 54 (10) (2015) 2757–2764, https://doi.org/10.1080/19443994.2014.903524.
[11] M.Z. Khan, S. Singh, T.R. Sreekrishnan, S.Z. Ahammad, Feasibility study on anaerobic biodegradation of azo dye reactive orange 16, RSC Adv. 4 (87) (2014) 46851–46859, https://doi.org/10.1039/c4ra06716a.
[12] B. Mu, A. Wang, Adsorption of dyes onto palygorskite and its composites: a review, J. Environ. Chem. Eng. 4 (1) (2016) 1274–1294, https://doi.org/10.1016/j.jece.2016.01.036.
[13] F. Sancenón, L. Pascual, M. Oroval, E. Aznar, R. Martínez-Máñez, Gated silica mesoporous materials in sensing applications, ChemistryOpen 4 (4) (2015) 418–437, https://doi.org/10.1002/open.201500053.
[14] Z.A. ALOthman, A review: fundamental aspects of silicate mesoporous materials, Materials 5 (2012) 2874–2902, https://doi.org/10.3390/ma5122874.
[15] C. Cheng, D. Lu, B. Shen, Y. Liu, J. Lei, L. Wang, J. Zhang, M. Matsuoka, Mesoporous silica-based carbon dot/TiO2 photocatalyst for efficient organic pollutant degradation, Microporous Mesoporous Mater. 226 (2016) 79–87, https://doi.org/10.1016/j.micromeso.2015.12.043.
[16] M. Zahid, K.A. Abd-Elsalam, Applications of Nanomaterials In Water Remediation: A Note From the Editors. In Aquananotechnology, Elsevier, 2021, pp. 1–10, https://doi.org/10.1016/B978-0-12-821141-0.00021-5.
[17] A.C. Chapman, A. Siebold, On the application of adsorption to the detection and separation of certain dyes, Analyst 37 (437) (1912) 339–345, https://doi.org/10.1039/an9123700339.
[18] W. Dong, J. Ding, W. Wang, L. Zong, J. Xu, A. Wang, Magnetic nano-hybrids adsorbents formulated from acidic leachates of clay minerals, J. Clean. Prod. 256 (2020), 120383, https://doi.org/10.1016/j.jclepro.2020.120383.
[19] F. Largo, R. Haounati, S. Akhouairi, H. Ouachtak, R. El Haouti, A. El Guerdaoui, et al., Adsorptive removal of both cationic and anionic dyes by using sepiolite clay mineral as adsorbent: experimental and molecular dynamic simulation studies, J. Mol. Liq. 38 (2020), 114247, https://doi.org/10.1016/j.molliq.2020.114247.
[20] S. Li, B. Mu, X. Wang, A. Wang, Recent researches on natural pigments stabilized by clay minerals: a review, Dyes Pigments 190 (2021), 109322, https://doi.org/10.1016/j.dyepig.2021.109322.
[21] K. Ramadass, G. Singh, K.S. Lakhi, M.R. Benzigar, J.H. Yang, S.H. Kim, A. M. Almajid, T. Belperio, A. Vinu, Halloysite nanotubes: novel and eco-friendly adsorbents for high-pressure CO_2 capture, Microporous Mesoporous Mater. (2019), https://doi.org/10.1016/j.micromeso.2018.10.035.
[22] M. Du, B. Guo, D. Jia, Newly emerging applications of halloysite nanotubes: a review, Polym. Int (2010), https://doi.org/10.1002/pi.2754.
[23] Q. Wang, J. Zhang, A. Wang, Alkali activation of halloysite for adsorption and release of ofloxacin, Appl. Surf. Sci. 287 (2013) 54–61, https://doi.org/10.1016/j.apsusc.2013.09.057.
[24] I. Pereira, M. Saleh, C. Nunes, S. Reis, F. Veiga, A.C. Paiva-Santos, Preclinical developments of natural-occurring halloysite clay nanotubes in cancer therapeutics, Adv. Coll. Interface Sci. 291 (2021), 102406, https://doi.org/10.1016/j.cis.2021.102406.
[25] M. Ding, H. Su, K. Yang, Y. Li, F. Li, B. Xue, Preparation and characterization of an aluminosilicate material with layer expansion structure, Appl. Clay Sci. 211 (2021), 106179, https://doi.org/10.1016/j.clay.2021.106179.
[26] G. Biddeci, G. Spinelli, P. Colomba, F. Di Blasi, Nanomaterials: a review about halloysite nanotubes, properties, and application in the biological field, Int. J. Mol. Sci. 23 (19) (2022) 11518, https://doi.org/10.3390/ijms231911518.
[27] L.W. Wong, P. Pasbakhsh, A.M. Arabi, J. Keeling, J.B.L. Tan, Halloysite nanotubes from various geological deposits: New insights to acid etching and their impacts on products' characteristics, J. Environ. Chem. Eng. 9 (5) (2021), 106235, https://doi.org/10.1016/j.jece.2021.106235.
[28] Lim S., Park S., Sohn D. (2020) Modification of halloysite nanotubes for enhancement of gas-adsorption capacity 68 189–196. https://doi.org/10.1007/s42860-019-00059-4.
[29] Q. Pan, N. Li, Y. Hong, H. Tang, Z. Zheng, S. Weng, Y. Zheng, L. Huang, Halloysite clay nanotubes as effective nanocarriers for the adsorption and loading of vancomycin for sustained release, RSC Adv. 7 (2017) 21352–21359, https://doi.org/10.1039/c7ra00376e.
[30] W. Liu, M. Fizir, F. Hu, A. Li, X. Hui, J. Zha, H. He, Mixed hemimicelle solid-phase extraction based on magnetic halloysite nanotubes and ionic liquids for the determination and extraction of azo dyes in environmental water samples, J. Chromatogr. A 1551 (2018) 10–20, https://doi.org/10.1016/j.chroma.2018.03.051.
[31] K.B. Shishkhanova, V.S. Molchanov, A.N. Baranov, E.P. Kharitonova, A.S. Orekhov, N.A. Arkharova, O.E. Philippova, A pH-triggered reinforcement of transient network of wormlike micelles by halloysite nanotubes of different charge, J. Mol. Liq. 370 (2023), 121032, https://doi.org/10.1016/j.molliq.2022.121032.
[32] S.K.S. Kushwaha, N. Kushwaha, P. Pandey, B. Fatma, Halloysite nanotubes for nanomedicine: Prospects, challenges and applications, BioNanoScience 11 (2021) 200–208, https://doi.org/10.1007/s12668-020-00801-6.
[33] T. Coultate, R.S. Blackburn, Food colorants: their past, present and future, Color. Technol. 134 (3) (2018) 165–186, https://doi.org/10.1111/cote.12334.
[34] F. Gosetti, V. Gianotti, S. Polati, M.C. Gennaro, HPLC-MS degradation study of E110 Sunset Yellow FCF in a commercial beverage, J. Chromatogr. A 1090 (1–2) (2005) 107–115, https://doi.org/10.1016/j.chroma.2005.07.024.
[35] M.M. Ghoneim, H.S. El-Desoky, N.M. Zidan, Electro-Fenton oxidation of Sunset Yellow FCF azo-dye in aqueous solutions, Desalination 274 (1–3) (2011) 22–30, https://doi.org/10.1016/j.desal.2011.01.062.
[36] M.G. Ravandi, M.R. Fat'hi, Green effervescence assisted dispersive liquid–liquid microextraction based on a hydrophobic deep eutectic solvent for determination of Sunset Yellow and Brilliant Blue FCF in food samples, New J. Chem. 42 (18) (2018) 14901–14908, https://doi.org/10.1039/c8nj00782a.
[37] F.P. De Sá, B.N. Cunha, L.M. Nunes, Effect of pH on the adsorption of Sunset Yellow FCF food dye into a layered double hydroxide (CaAl-LDH-NO_3), Chem. Eng. J. 215 (2013) 122–127, https://doi.org/10.1016/j.cej.2012.11.024.
[38] S. Foroughirad, V. Haddadi-Asl, A. Khosravi, M. Salami-Kalajahi, Synthesis of magnetic nanoparticles-decorated halloysite nanotubes/poly([2-(acryloyloxy) ethyl]trimethylammonium chloride) hybrid nanoparticles for removal of Sunset Yellow from water, J. Polym. Res. 27 (2020), 320, https://doi.org/10.1007/s10965-020-02293-0.
[39] Y.J. Ai, P. Liang, Y.X. Wu, Q.M. Dong, J.B. Li, Y. Bai, B.J. Xu, Z. Yu, D. Ni, Rapid qualitative and quantitative determination of food colorants by both Raman spectra and Surface-enhanced Raman Scattering (SERS), Food Chem. 241 (2018) 427–433, https://doi.org/10.1016/j.foodchem.2017.09.019.
[40] Y. Lu, H. Zhao, X. Huang, D. Hu, Y. Wu, X. Ba, H. Zhang, Exploring maleimide-anchored halloysites as nanophotoinitiators for surface-initiated photografting strategies, Chem. Commun. 58 (2022) 13636–13639, https://doi.org/10.1039/d2cc05339j.
[41] Y.P. Yew, K. Shameli, M. Miyake, N.B.B.A. Khairudin, S.E.B. Mohamad, H. Hara, F. B.M.N. Mariam, K.X. Lee, An eco-friendly means of biosynthesis of superparamagnetic magnetite nanoparticles via marine polymer, IEEE Trans. Nanotechnol. 16 (6) (2017) 1047–1052, https://doi.org/10.1109/tnano.2017.2747088.
[42] J. Crangle, G.M. Goodman, The magnetization of pure iron and nickel, Proc. Royal Soc. London. Math. Phys. Sci. 321 (1547) (1971) 477–491, https://doi.org/10.1098/rspa.1971.0044.

[43] R.D. White, D.V. Bavykin, F.C. Walsh, The stability of halloysite nanotubes in acidic and alkaline aqueous suspensions, Nanotechnology 23 (6) (2012), 065705, https://doi.org/10.1088/0957-4484/23/6/065705.
[44] S. Park, J. Ryu, H.Y. Cho, D. Sohn, Halloysite nanotubes loaded with HKUST-1 for CO_2 adsorption, Colloids Surf. A: Physicochem. Eng. Asp. 651 (2022), 129750, https://doi.org/10.1016/j.colsurfa.2022.129750.
[45] E.C. Stoner, E.P. Wohlfarth, A mechanism of magnetic hysteresis in heterogeneous alloys, Philos. Trans. R. Soc. Lond. Ser. A, Math. Phys. Sci. 240 (826) (1948) 599–642, https://doi.org/10.1098/rsta.1948.0007.